Green Chemistry

ROYAL SOCIETY OF CHEMISTRY

PAPER

View Article Online
View Journal | View Issue

Cite this: *Green Chem.*, 2023, **25**, 3117

Electrocatalytic amino acid synthesis from biomass-derivable keto acids over ball milled carbon nanotubes†

Yiying Xiao,[a,b] Chia Wei Lim,[b] Jinquan Chang,[a,b] Qixin Yuan,[b] Lei Wang *[b] and Ning Yan *[a,b]

Received 24th January 2023,
Accepted 17th March 2023

DOI: 10.1039/d3gc00265a

rsc.li/greenchem

Electrocatalytic reductive amination (ERA) offers an attractive way to synthesise organonitrogen chemicals from renewable feedstocks. Here, we report carbon nanotubes (CNTs) as an effective catalyst for the ERA of biomass-derivable α-keto acids into amino acids using NH_3 as the nitrogen source. Through a facile ball milling (BM) treatment, the intrinsic defects in the CNTs were increased while the electrocatalytic activity of CNTs converting 2-ketoglutaric acid into glutamic acid was enhanced by approximately seven times. A high faradaic efficiency (FE) of ∼90% with a corresponding glutamic acid formation rate of up to 180.9 mmol g^{-1}_{cat} h^{-1} was achieved, and ∼60% molar yield of glutamic acid was obtained after 8 h of electrolysis. Electrokinetic analyses indicated that the BM–CNT catalysed ERA exhibits a first-order dependence on the substrate and NH_3, with a rate-determining step (RDS) involving the first electron transfer. Following this protocol, a number of amino acids were prepared with moderate to high FEs and formation rates. Significantly, we synthesised long carbon chain amino acids, which are typically obtained in lower yields using the existing methods.

Introduction

Amino acids are essential compounds used in a myriad of industrial applications, including human food, animal feed, pharmaceutical products, bio-based polymer synthesis and so on.[1–3] Currently, amino acid production mainly relies on microbial fermentation processes, which suffer from a long culturing time, complicated and energy intensive separation/purification, and the need for single-use enzymes that can be costly.[4,5] Chemical methods such as the Strecker reaction,[6] the Gabriel synthesis,[7] and the Miller experiment[8] may offer higher space–time productivities, but they usually employ toxic feedstocks or harsh reaction conditions, hindering practical applications.

The construction of the C–N bond through thermocatalytic reductive amination provides amino acids from keto acids and a nitrogen source under comparatively mild conditions.[9,10] This pathway involves a two-step procedure as illustrated in Scheme 1: a carbonyl compound and a nitrogen source (*e.g.*, NH_3) first condense to form an imine intermediate which is subsequently reduced to afford an amine product, while the direct reduction of the carbonyl compound is usually the competing side reaction. The selective reduction of imines can be achieved by using reducing agents such as formates,[11,12] silanes,[13] and hydrides,[14–16] which generate organic waste and

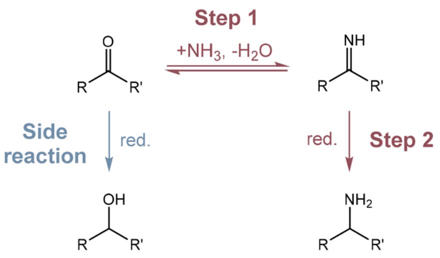

Scheme 1 The reaction pathway of reductive amination. Step 1: condensation of a carbonyl compound and a nitrogen source to form an imine intermediate. Step 2: reduction of the imine intermediate to afford an amine product. Side reaction: reduction of the carbonyl compound to form a hydroxyl compound.

---

[a] *Joint School of National University of Singapore and Tianjin University, International Campus of Tianjin University, Binhai New City, Fuzhou 350207, China. E-mail: ning.yan@nus.edu.sg*

[b] *Department of Chemical and Biomolecular Engineering, National University of Singapore, Singapore 117585, Singapore. E-mail: wanglei8@nus.edu.sg*

† Electronic supplementary information (ESI) available: TEM images, SEM images, XRD patterns, XPS spectra, NMR spectra, contact angles, pH effects, formation rates of 2-hydroxyglutaric acid, CV curves, LSV curves, kinetic modelling, electrochemical setup, schemes, a table of comparison of the electrocatalytic amino acid synthesis from keto acids in this work with those in the literature, a table of the BET surface area of various CNTs, and a table of the specifications of the CNT materials. See DOI: **https://doi.org/10.1039/d3gc00265a**

require solvent clean-up. Molecular H_2 is also commonly used for reductive amination in the presence of Ni-based catalysts[17,18] or noble metal-based catalysts, including Pt,[19] Pd,[20] Ru,[21,22] Rh,[23] and Ir.[24] Although more environmentally friendly than other reductants, H_2 still has several disadvantages of (1) needing to be generated from other energy sources; (2) requiring relatively severe reaction conditions (*e.g.*, 10 bar H_2, 80 to 150 °C), and (3) being able to hydrogenate other functional groups such as carbonyl groups or aromatic rings depending on the property of the catalysts.

In recent years, the electrochemical valorisation of biomass derivatives to value-added chemicals has emerged as a new frontier.[25–31] As an example, electrocatalytic reductive amination (ERA), occurring *via* the pathway shown in Scheme 1, has several advantages. Similar to other well studied electrocatalytic reactions including CO_2/CO reduction,[32–36] N_2 reduction[37–40] and O_2 reduction[41–43] reactions, it proceeds under environmentally benign conditions, using electrons as reductants and water as the hydrogen source. Additionally, the selectivity of ERA can be facilely controlled by altering the applied potentials. As an early example, Meisters *et al.* prepared several amino acids from the corresponding α-keto acids in aqueous NH_3/NH_4Cl solution, with yields ranging from 24% to 88% after long-time constant potential electrolysis.[44,45] Recently, Choi *et al.* investigated the ERA of 5-hydroxymethylfurfural (5-HMF) with methylamine, achieving high faradaic efficiency (FE) and selectivity by using a high surface area Ag electrode.[46] In 2021, Palkovits and co-workers discovered that Cu was a highly selective cathode material to convert levulinic acid to 1,5-dimethyl-2-pyrrolidone in 78% yield through ERA and dehydration.[47] These works often relied on toxic and/or expensive metals as the main component in the catalyst. For metal oxide based catalyst, Yamauchi *et al.* synthesised seven amino acids with FEs of 77–99% using TiO_2, but hydroxylamine (NH_2OH) was used as the nitrogen source, which is more poisonous and costly than NH_3.[48,49] Interestingly, Sun *et al.* demonstrated that ERA using the same catalyst could be combined with alcohol oxidation to obtain amino acids directly from alcohols.[50]

Carbon materials have been recognised as prospective catalysts in diverse electrochemical processes including O_2 reduction,[51–53] CO_2 reduction,[54–57] and organic electrosynthetic reactions.[58,59] The electrocatalytic reactivity of carbon materials is tuneable by defect engineering, heteroatomic doping, and surface functional group modification. Herein, we have extended the electrocatalytic application of carbon nanotubes to convert biomass-derivable α-keto acids into the corresponding amino acids with moderate to high formation rates and FEs (Fig. 1). Ball milling (BM) treatment has been identified as an effective strategy to introduce intrinsic defects into CNTs to substantially boost the activity of ERA. We also systematically investigated the influences of applied potentials and substrate/ammonia concentrations on the FE and formation rate of glutamic acid, as well as catalyst recycling.

Materials and methods

Chemicals and materials

Multi-walled carbon nanotubes (bulk CNTs, MA-EN-CO-0R0113) were purchased from Canrd Co., Ltd. N-doped multi-walled carbon nanotubes (N–CNTs, XFM63) and amino-modified multi-walled carbon nanotubes (CNT–NH_2, XFM62) were purchased from Nanjing XFNANO Materials Tech Co., Ltd. The specifications of the CNT materials are provided (Table S3†). Carbon paper (TGP-H-060) was purchased from Suzhou Sinero Tech Co., Ltd. The Ag/AgCl electrode (3 M KCl) and graphite rod were purchased from

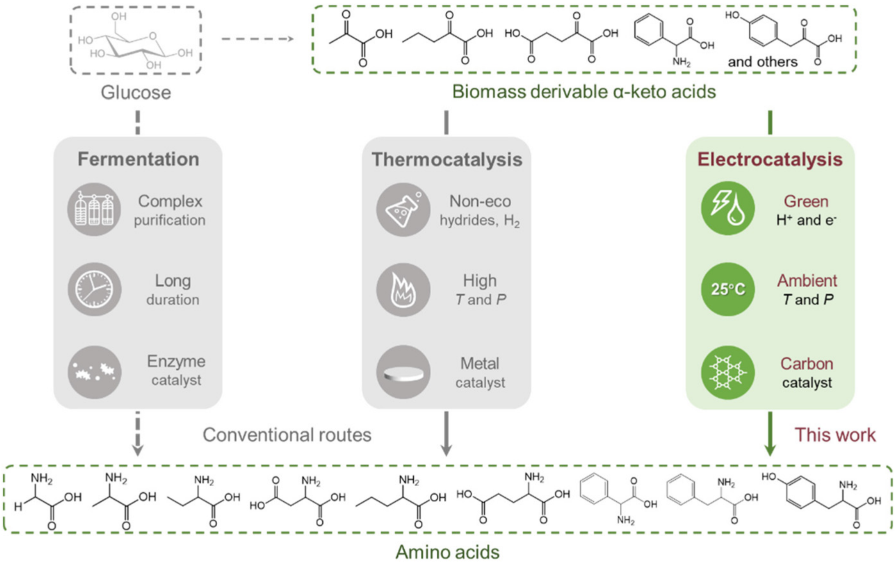

Fig. 1 Comparison of the amino acid synthesis protocols *via* bio-, thermal-, and electrocatalytic routes.

Shanghai Jingchong Electronic Technology Development Pte. Ltd. The Nafion 117 membrane (N117, DuPont) was purchased from Xianfeng Instrument Tech Co., Ltd. Nitrogen gas (N_2, 99.9995%) was supplied by Air Liquide. Sodium chloride (NaCl, ≥99.0%), silver nitrate ($AgNO_3$, ≥99.0%), Nafion® perfluorinated resin solution (5 wt% in 45% water balanced with lower aliphatic alcohols), ammonium sulfate ($(NH_4)_2SO_4$, ≥99.0%), ammonia solution (~25 wt% NH_3 in water), pyruvic acid (98%), glyoxylic acid solution (50 wt% in water), 2-ketobutyric acid (97%), oxaloacetic acid (97%), 2-oxovaleric acid (98%), 2-ketoglutaric acid (99.0–101.0%), phenylglyoxylic acid (97%), sodium phenylpyruvate, 4-hydroxyphenyl pyruvic acid (98%), L-glutamic acid (≥99.0%) and 3-(trimethylsilyl)-1-propanesulfonic acid sodium salt (97%) were supplied by Sigma-Aldrich. Nitric acid (HNO_3, 65%) and absolute ethanol (>99.7%) were supplied by VWR Chemicals. Acetone (HPLC grade) was purchased from Fisher Chemical. Deuterium oxide (D_2O, D, 99.9%) was purchased from Cambridge Isotope Laboratories. Except for bulk CNTs, N–CNTs and CNT–NH_2, commercially available chemicals were used as received without purification. All aqueous solutions were prepared using ultra-pure water (Milli-Q®, conductivity of 0.056 μS cm^{-1}).

Catalyst preparation

Bulk CNTs, N–CNTs and CNT–NH_2 were separately sonicated in ultra-pure water and acetone (three times in each solvent) to remove impurities. After the removal of the supernatant by centrifugation, the precipitate was dried at 80 °C overnight. In a typical fabrication procedure of ball-milled CNTs (BM–CNTs), 0.1 g of bulk CNT powder together with 0.5 g of NaCl and 10 g of zirconium oxide (ZrO_2) balls was introduced to a zirconium oxide ball-mill chamber (45 mL). Ball milling (Pulverisette 7, Fritsch) was carried out at 300 rpm for 1, 2, 3, 4 and 5 hours. The ball milling process was paused for 10 min after every 20 min of grinding to avoid overheating. After ball milling, the powder mixture was separated from the balls using a steel mesh. It was washed with ultra-pure water and vacuum-filtered until there was no precipitate in the filtrate when $AgNO_3$ was added. Then, the collected powder was oven-dried at 80 °C overnight, resulting in the BM*X* h–CNT (where *X* represents the number of hours of the ball milling process).

Electrochemical measurements

Carbon paper cut into 1.5 × 3 cm was pre-treated by immersing it in 1 M nitric acid and sonicating for 30 min. Following this step, the carbon paper was washed thoroughly with ultra-pure water and absolute ethanol, and then dried at 80 °C overnight. To prepare the catalyst ink, 4.5 mg of the prepared catalyst was dispersed in a mixture of 1.2 mL of absolute ethanol and 10 μL of Nafion® perfluorinated resin solution and then sonicated for 1.5 hours to form a homogeneous suspension. The working electrode was prepared by dropping the catalyst ink onto both sides of a pre-treated carbon paper.

All the electrochemical measurements were performed with an electrochemical workstation (CHI 760E, CH Instruments Ins), except for the electrochemical impedance spectroscopy (EIS) tests, which were carried out using a Gamry Reference 3000 potentiostat. The measurements were carried out in a two-compartment (H-type) electrochemical cell with a three-electrode configuration at room temperature under stirring, except for the cyclic voltammetry (CV) tests which were conducted without stirring. A graphite rod and an Ag/AgCl electrode (3 M KCl) were used as the counter and reference electrodes, respectively. $NH_3/(NH_4)_2SO_4$ buffers ($[NH_3]/[NH_4^+] = 1$, pH 10) with and without organic substrates were used as the cathodic and anodic electrolyte solutions, respectively. The two compartments (50 mL each), each containing 40 mL of electrolytes, were sealed with Teflon caps and separated with a piece of Nafion 117 membrane (Fig. S18†). In all cases, the cathodic electrolyte solution was purged with purified nitrogen gas for 30 min at the start of each experiment to remove atmospheric air. During the measurements, nitrogen gas was continuously bubbled into the cathodic electrolyte. Every measurement, except for the stability test, was carried out on a freshly prepared working electrode. The potentials applied against the Ag/AgCl reference electrode were converted to the *iR*-corrected reversible hydrogen electrode (RHE) scale on the basis of the following equation:

$$E_{\mathrm{RHE}}\ (\mathrm{V}) = E_{\mathrm{Ag/AgCl}}\ (\mathrm{V}) + 0.210\ \mathrm{V} + 0.059\ \mathrm{V} \times \mathrm{pH} - iR$$

R is the bulk electrolyte resistance between the working electrode and the reference electrode, which was calculated based on the potentiostatic EIS data fitted with a constant phase element (CPE) circuit. The value of *R* was about 0.2 Ω for all experiments. Current densities were calculated according to the detected currents and geometric area of the working electrode (4.5 cm^2).

The electrosynthesis of amino acids was carried out at a constant potential and investigated systematically using different working electrodes, potentials, substrate concentrations, ammonia concentrations and substrates. The linear sweep voltammetry (LSV) measurements were conducted from −0.6 V to −1.45 V *versus* Ag/AgCl at a scan rate of 20 mV s^{-1} with and without substrates with different working electrodes. The CV measurements were performed from 0.2 V to −1.35 V *versus* Ag/AgCl at scan rates ranging from 10 to 200 mV s^{-1} under various conditions. The potentiostatic EIS measurements were performed at frequencies ranging from 10^6 to 0.1 Hz with an RMS amplitude of 10 mV at −1.1 V *versus* Ag/AgCl.

Product identification and quantification

The reaction solution collected from the cathodic compartment was analysed by ^1H nuclear magnetic resonance (NMR) spectroscopy using a Bruker Ascend™ 400 (400 MHz) at room temperature with water suppression. The anodic compartment was also analysed, confirming that the Nafion 117 membrane was in a good condition. Typically, 300 μL of the electrolyte was mixed with 300 μL of deuterium oxide containing 20 mM 3-(trimethylsilyl)-1-propanesulfonic acid sodium salt, which was used as an internal standard. The amino acids and corresponding hydroxy acids were identified from the signals at approximately 3.4–3.8 ppm and 4.0–4.2 ppm assignable to the proton on the α-carbon of the amino acids and hydroxy acids, respectively (Fig. S11,† all presented data are the average results of 8 scans). For quantification, the concentration of each compound could be calculated from the equation of the calibration curve (Fig. S12† as an example) since the concentration of amino acids or hydroxy acids exhibits a linear relationship with the integral area of the characteristic peak. More specifically, the integral value of the peak corresponding to the product was obtained assuming that the integral value of the internal standard peak was 1.0000.

The faradaic efficiency (FE) for each compound was calculated as follows:

$$\mathrm{FE}(\%) = \frac{n \times C \times V \times F}{Q} \times 100$$

where n is the number of electrons required for the formation of the products ($n = 2$), C is the molar concentration of the products, V is the volume of the electrolyte (0.04 L), F is the Faraday constant (96 485 C mol^{-1}), and Q represents the total charge passed during the electrolysis.

Material characterisation

The defective level of the CNT materials was determined using a Raman microscope (HORIBA Jobin Yvon) with a 633 nm excitation laser. The chemical environments of the CNT materials were identified by X-ray photoelectron spectroscopy (XPS, Kratos AXIS Ultra$^{\mathrm{DLD}}$, Kratos Analytical Ltd) with a mono Al Kα X-ray source. All XPS data were calibrated to C 1s (C–C bond) at 284.80 eV and analysed using the Vision Processing and XPSPEAK Version 4.1 software. X-ray diffraction (XRD) analysis was performed using a diffractometer (Bruker D8 Advance), where 2θ ranged from 10° to 80° at a scan speed of 5° min^{-1} with a step size of 0.02°, to study the crystal structure of the CNT materials. The surface morphology and microstructure of the CNT materials were characterised using a field emission scanning electron microscope (FESEM, JEOL JSM-7610F) operating at 5 kV and a field emission transmission electron microscope (FETEM, JEOL JEM-2100F) operating at 200 kV. The specific surface areas of different CNT materials were measured by nitrogen adsorption/desorption based on the Brunauer–Emmett–Teller (BET, NOVAtouch NT 4LX-1) method. About 200 mg of samples were degassed in nitrogen at 150 °C for 6 hours before analysis. The contact angles for carbon paper and BM3 h–CNT covered carbon paper were measured using a Krüss G10 contact angle measurement system.

Results and discussion

Characterisation of the electrocatalysts

The surface morphology of CNTs was characterised before and after the ball milling treatment by transmission electron microscopy (TEM) and scanning electron microscopy (SEM). As illustrated in the TEM image (Fig. 2a), most of the bulk CNTs were curved, entangled and twisted, together with the end tips almost closed. After 3 h of ball milling (sample denoted as BM3 h–CNT), a large portion of CNTs was cut shorter with open ends, while plenty of individual CNTs were separated from the agglomerates (Fig. 2b). It could also be observed that the destroyed walls were kinked and discontinuous with a multilayer polyaromatic carbon structure present in certain parts (Fig. 2b, arrow and Fig. S1 and S3†), implying structural defects and graphitic disorder in the CNT sample. Consistent with the TEM results, the SEM images show that the agglomeration of CNTs was markedly reduced after ball milling, while amorphous carbon was sporadically observed on the surface of CNTs (Fig. S2†).

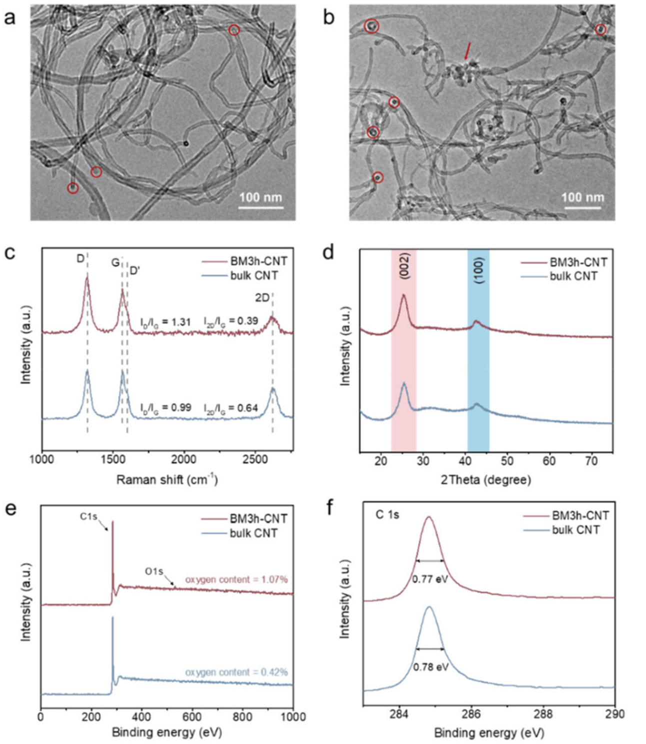

Fig. 2 Characterisation of pristine and ball milled CNT. TEM images of (a) bulk CNT and (b) BM3 h–CNT. The red circles and arrows highlight the end tips and amorphous structure of the CNTs, respectively. (c) Raman spectra of bulk CNT and BM3 h–CNT. The values of I_D/I_G and I_{2D}/I_G are averages calculated based on three independent measurements. (d) XRD patterns of bulk CNT and BM3 h–CNT. The peaks at around 25.4° and 42.6° are attributed to the (002) graphite plane reflection and the (100) in-plane reflection, respectively. (e) XPS survey spectra of bulk CNT and BM3 h–CNT. (f) XPS high resolution C 1s spectra of bulk CNT and BM3 h–CNT.

In the Raman spectra, four characteristic peaks were identified at around 1321 cm^{-1}, 1602 cm^{-1}, 1566 cm^{-1} and 2620 cm^{-1}, which correspond to the disordered D and D′ bands, graphitic G band and graphene-layer-sensitive 2D band, respectively (Fig. 2c). The intensity ratio of the D band to the G band (I_D/I_G), reflecting the defective level of carbon materials,[60] increased from 0.99 in bulk CNTs to 1.31 in BM3 h–CNTs, demonstrating the existence of a more defective structure and disordered phase in the latter. Additionally, the declining 2D/G intensity ratios (I_{2D}/I_G) from 0.64 to 0.39 after ball milling suggests that there were less graphene layers in BM3 h–CNTs compared with those in bulk CNTs,[61] which is consistent with the observation in the high resolution TEM images (Fig. S3†).

The XRD patterns of the samples exhibit two characteristic peaks of CNT materials. There were no observable changes in the XRD patterns after ball milling (Fig. 2d and Fig. S4†), indicating that the ball milling treatment has no significant effects on the crystal structure of the CNTs. As displayed in the XPS survey spectra (Fig. 2e), only C and a small amount of O (oxygen contents of 0.42% and 1.07% in bulk CNTs and BM3 h–CNTs, respectively) were detected, demonstrating that the ball milling treatment does not introduce non-oxygen heteroatom elements into CNTs. The high-resolution C 1s spectra of BM3 h–CNTs and untreated CNTs are nearly identical, with similar Full Width at Half Maximum (FWHM) values of 0.77 eV (Fig. 2f). The XPS spectra of CNTs after different durations of ball milling treatment are provided in Fig. S5.†

Electrocatalytic reductive amination of 2-ketoglutaric acid to glutamic acid

We initially examined the characteristics of electrocatalytic reductive amination by linear sweep voltammetry (LSV) using 2-ketoglutaric acid as a model compound. The polarisation curve in the absence of 2-ketoglutaric acid was ascribed to the hydrogen evolution reaction (HER) (Fig. 3a, grey line). Upon the addition of 2-ketoglutaric acid, there was a dramatic shift in the onset potential in the positive direction together with a steep increase in the current density, indicating that the electrocatalytic reductive amination is favoured over HER on CNTs. Compared to bulk CNTs (blue line), BM3 h–CNTs exhibited substantially enhanced electrocatalytic performance reflected by the much higher cathodic current density (violet line). It is also worth emphasising that two irreversible reduction peaks, around −0.2 V *vs.* reversible hydrogen electrode (RHE) and −0.5 V *vs.* RHE, were observed in the cyclic voltammetry (CV) curves when 2-ketoglutaric acid was added (Fig. 3b), attributable to the reduction of the 2-iminoglutaric acid intermediate (forming the target compound, glutamic acid) and 2-ketoglutaric acid (forming the side product, 2-hydroxyglutaric acid), respectively.[44,62–64] This suggests that the selectivity towards glutamic acid or 2-hydroxyglutaric acid can be effectively tuned by altering the applied potentials when ball milled CNTs are used as the electrode.

Next, the effects of different applied potentials, substrate/ammonia concentrations and pH on the FE and glutamic acid formation rate (GLU formation rate) were investigated (Fig. 3c–e, Fig. S8 and S9†). As the applied potential varied from −0.2 to −0.6 V *vs.* RHE, the formation rate of glutamic acid first increased from 4.6 to 172.4 mmol g^{-1}_{cat} h^{-1} and began to level off when the potential was more negative than −0.39 V *vs.* RHE (Fig. 3c). In the range of −0.2 to −0.3 V *vs.* RHE, only glutamic acid was detectable, with the FE showing an upward trend as the potential became more negative and reaching its highest value (93.1%) at −0.25 V *vs.* RHE. In agreement with earlier CV

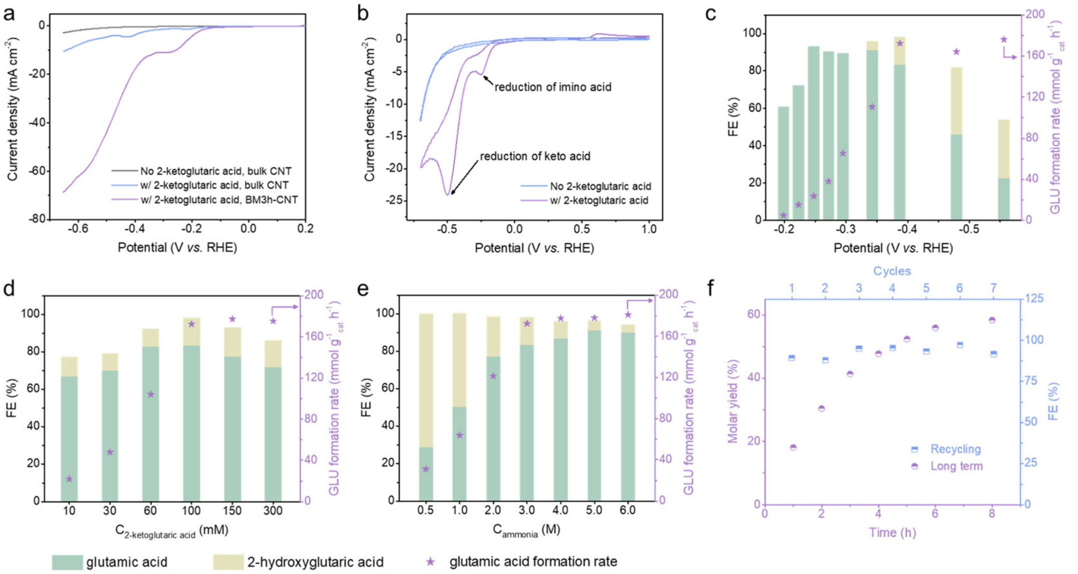

Fig. 3 Electrocatalytic reductive amination of biomass-derivable 2-ketoglutaric acid to glutamic acid. (a) LSV curves of bulk CNTs without (grey line) and with (blue line) 100 mM 2-ketoglutaric acid, and BM3 h–CNTs with 100 mM 2-ketoglutaric acid (violet line) in a 3 M NH_3/NH_4^+ buffer (pH 10) at a scan rate of 20 mV s^{-1} at room temperature. (b) CV curves of BM3 h–CNT without (blue line) and with (violet line) 100 mM 2-ketoglutaric acid in a 3 M NH_3/NH_4^+ buffer (pH 10) at a scan rate of 10 mV s^{-1} at room temperature. The FE and GLU formation rate in the BM3 h–CNT catalysed room-temperature constant potential electrolysis of 2-ketoglutaric acid for 1 h at different (c) applied potentials (100 mM 2-ketoglutaric acid, 3 M NH_3, pH 10), (d) 2-ketoglutaric acid concentrations (−0.39 V *vs.* RHE, 3 M NH_3, pH 10) and (e) NH_3 concentrations (−0.39 V *vs.* RHE, 100 mM 2-ketoglutaric acid, pH 10). (f) Extended duration room-temperature electrolysis (violet dots) and recycling test (blue dots) over BM3 h–CNTs with 100 mM 2-ketoglutaric acid, 6 M NH_3 (pH 10) at −0.39 V *vs.* RHE. For recycling experiments, the reaction time was 1 h.

analyses, the FE towards glutamic acid declined sharply at potentials more negative than −0.39 V *vs.* RHE, while the FE for 2-hydroxyglutaric acid displayed a significant increase as the keto acid reduction became more favourable.

The impact of reactant concentrations ($C_{\text{2-ketoglutaric acid}}$ and C_{ammonia}) on glutamic acid synthesis was investigated at −0.39 V *vs.* RHE (Fig. 3d and e). As the concentration of 2-ketoglutaric acid increased, the glutamic acid formation rate showed a remarkable increase before increasing at a slower pace. The plateau of the glutamic acid formation rate can be rationalised by the possibility that the active sites on the cathode were saturated by the reactants. There was a moderate decline of FE for glutamic acid when the concentration of 2-ketoglutaric acid was higher than 100 mM (Fig. 3d). Possible reasons for the drop in FE include the formation of dimers or oligomers which also participate in reduction reactions (Scheme S1a,† electrons were utilised, but the products were not quantified) and/or the condensation between the substrate and product (Scheme S1b†), based on NMR analysis (Fig. S10†).[44,46] Due to the shifted ketone–imine equilibrium to the imino acid side, the FE for glutamic acid showed a sharp increase from 28.8% to 91.2% when the ammonia concentration increased from 0.5 M to 5 M (Fig. 3e). The production of glutamic acid was found to be favoured at high pH, which similarly promotes the shifting of the ketone–imine equilibrium to produce more imino acid (Fig. S8†). Altogether, a high FE of ~90% and a corresponding formation rate of 180.9 mmol g^{-1}_{cat} h^{-1} for glutamic acid synthesis were achieved under the optimum reaction conditions: 100 mM 2-ketoglutaric acid, 6 M ammonia and pH 10 at an applied potential of −0.39 V *vs.* RHE.

An extended duration electrosynthesis was conducted on BM3 h–CNTs under the optimised conditions; nearly 60% molar yield of glutamic acid was obtained after 8 h of electrolysis (Fig. 3f, violet dots). In the recycling experiments, no obvious performance loss was observed even after seven repetitions (Fig. 3f, blue dots), highlighting the durability of the catalyst. Overall, the BM3 h–CNT catalyst exhibited a high current density, FE, GLU formation rate and yield achieved at a relatively low overpotential in a relatively short reaction time, which are comparable or superior to the those of catalysts reported elsewhere[44,45,48,49,62] (Table S1†).

Correlation of CNT structure and electrocatalytic reductive amination reactivity

A series of CNTs prepared by varying the ball milling duration and two types of N configurated CNTs (N–CNT and CNT–NH_2) were comparatively studied. As displayed in Fig. 4a, the specific surface area (Table S2†) normalised GLU formation rate (denoted as the GLU formation rate$_{\text{BET surface area}}$) increased substantially with increasing milling time between 0 and 3 h, followed by a downward trend when the milling time exceeded 3 h. Decreased electrical conductivity (Fig. 4d) and clear structural deterioration of the CNTs (Fig. S1 and S2†) were observed in the samples after long time ball milling treatment, which are likely to be the reasons for their lower activity. The FE towards glutamic acid increased after the ball milling treatment and remained constant at around 85% with prolonging milling time. No obvious relationships between the catalytic performance and the CNT morphology (Fig. S1 and S2†), crystallinity (Fig. S4†) and functionality (Fig. S5†) were observed.

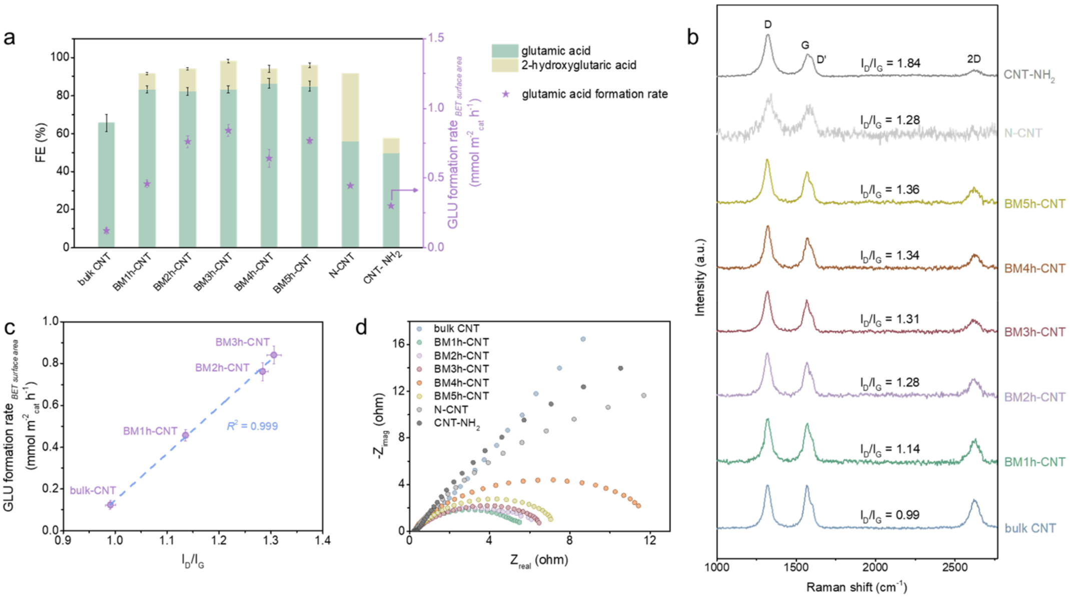

Fig. 4 Correlation of glutamic acid synthesis activity and CNT structure. (a) FE and GLU formation rate$_{\text{BET surface area}}$ of room-temperature electrolysis of 100 mM 2-ketoglutaric acid and 3 M NH_3 (pH 10) at −0.39 V *vs.* RHE for 1 h with different CNT materials. (b) Raman spectra of various CNT materials. (c) Correlation of CNT defective level I_D/I_G and surface area normalised glutamic acid formation rate. (d) Electrochemical Impedance Spectra (EIS) Nyquist plots of various CNT materials at −0.29 V *vs.* RHE in 100 mM 2-ketoglutaric acid and 3 M NH_3/NH_4^+ buffer (pH 10) solutions. The error bars denote the standard deviation of data from three independent experiments.

On the other hand, the effect of the defective degree of the CNTs was much more profound on the reaction. In accordance with the trend of the electrocatalytic activity, the D band intensity and the I_D/I_G ratio of the BM–CNTs increased progressively with increasing milling time (Fig. 4b); the GLU formation $\text{rate}_{\text{BET surface area}}$ was linearly correlated with the I_D/I_G ratio of the CNTs (R^2 = 0.999, Fig. 4c), implying that the intrinsic carbon defects in CNTs potentially serve as the active sites and contribute to the high activity in ERA.

Despite having high I_D/I_G ratios (Fig. 4b), interestingly, the N configurated CNTs exhibited relatively low GLU FE and formation $\text{rate}_{\text{BET surface area}}$ compared with BM–CNTs (Fig. 4a). N–CNTs even displayed a relatively higher FE towards the by-product, 2-hydroxyglutaric acid, compared with BM–CNTs and CNT–NH_2. According to the characterisation results (Fig. S6 and S7†), we speculate that the causes for the inferior performance of the N configurated CNTs towards ERA are: (1) the low charge transfer efficiency of N–CNTs and CNT–NH_2 (Fig. 4d) owing to the graphene lattice distortion by N heteroatoms and (2) the high amounts of pyridinic N and pyrrolic N in N–CNTs (Fig. S6f†) that may be favourable for the reduction of the C═O double bond[65–69] rather than the C═N double bond. As the high defective degrees for N–CNTs and CNT–NH_2 are due to the incorporation of extrinsic N defects,[70] these control samples further highlight the important role of the intrinsic defects in CNTs for the reductive amination.

Investigation of glutamic acid synthesis mechanism

The formation of glutamic acid followed first order dependence with respect to both 2-ketoglutaric acid and ammonia at low concentrations, but approached zeroth order dependence at 2-ketoglutaric acid concentrations above 100 mM and ammonia concentrations above 3 M (Fig. 5a and b). As displayed in Fig. 5c, the Tafel slope of BM3 h–CNTs in the region of glutamic acid production was 113.2 mV dec^{-1}, implying that the rate determining step (RDS) for the overall reaction is the first electron transfer process. Kinetic modelling was also conducted to verify the observed reaction orders and our proposed RDS, showing a good agreement between the model predictions and the experimental results (Fig. S13†). In the literature, there are mainly two possible mechanisms for ERA in aqueous electrolytes. The first one, as previously found on mercury, is characterised by an initial direct electron addition to the imino acid[44] (Scheme S2a†). The second mechanism involves the initial formation of a hydride on the cathode surface, followed by the addition of a hydrogen atom to the imino acid, which often happens on metals with low HER overpotentials, such as platinum and palladium[45] (Scheme S2b†). In our system, the CV curve of 2-ketoglutaric acid displayed in Fig. 3b shows a peak at around −0.2 V *vs.* RHE, attributable to the electron transfer to the imino acid.[44,62–64] Furthermore, the observed Tafel slope of 113.2 mV dec^{-1} rules out a pathway through hydride formation as its RDS may involve the adsorption of the imino acid on the cathode surface,[45] resulting in a theoretical Tafel slope of 60 mV dec^{-1}. Thus, the ERA on BM3 h–CNTs is likely to occur through the direct electron transfer pathway.

Taken together, the electrokinetic study suggests the following BM3 h–CNT catalysed ERA mechanism (Scheme 2): firstly, a nucleophilic attack by ammonia on a keto acid **A** results in a 2-amino-2-hydroxy acid **B**, followed by the elimination of a water molecule to afford an imino acid intermediate **C**. Subsequently, the *in situ* formed imino acid directly accepts an electron at the electrode surface to form a radical anion **D**, which extracts a proton from water to generate a radical **E**. **E** then undergoes a fast proton-coupled electron transfer to form an amino acid **F** at the cathode surface.

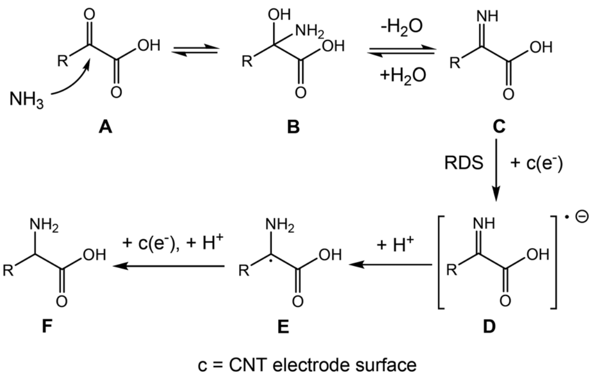

Scheme 2 Proposed mechanism for the BM3 h–CNT catalysed ERA.

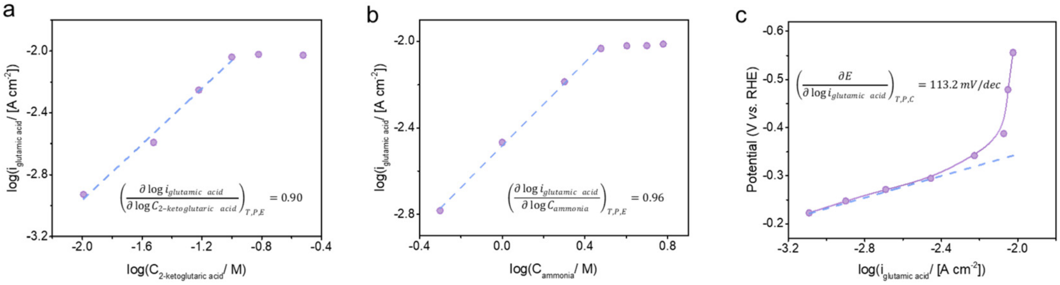

Fig. 5 Kinetic analyses of BM3 h–CNT catalysed electro-reductive amination of 2-ketoglutaric acid to glutamic acid. The dependence of the glutamic acid partial current density on the concentration of (a) 2-ketoglutaric acid (3 M ammonia) and (b) ammonia (100 mM 2-ketoglutaric acid) at −0.39 V *vs.* RHE, pH 10. (c) Tafel plot of glutamic acid synthesis with 100 mM 2-ketoglutaric acid and 3 M ammonia at pH 10.

Table 1 Electrocatalytic transformation of different biomass-derivable α-keto acids to the corresponding amino acids over BM3 h–CNTs

Entry	Substrate	Product Structure	Product Name	FE (%)	Formation rate (mmol g^{-1} h^{-1})
1	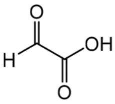	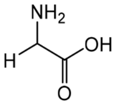	Glycine	87.4	16.6
2	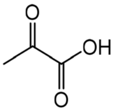	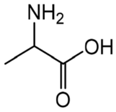	Alanine	45.0	43.3
3	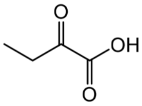	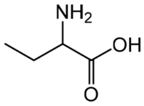	2-Aminobutyric acid	59.2	64.0
4	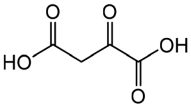	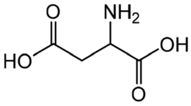	Aspartic acid	46.9	14.8
5	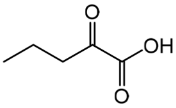	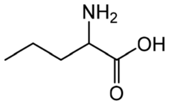	Norvaline	91.3	166.9
6	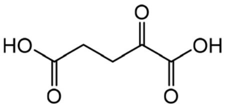	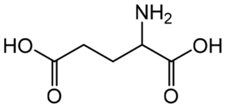	Glutamic acid	90.0	123.7
7	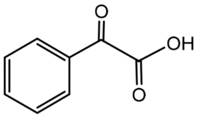	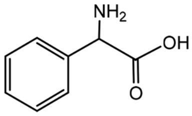	Phenylglycine[a]	31.4	46.8
8	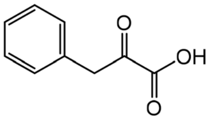	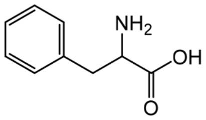	Phenylalanine[a]	92.8	45.9
9	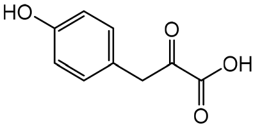	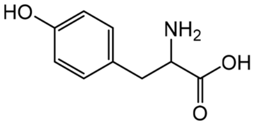	Tyrosine[a]	72.9	21.1

Reaction conditions: 4.5 mg of the catalyst, 60 mM substrate, 6 M ammonia, pH 10, −0.39 V *vs.* RHE, room temperature, 1 h reaction time. [a] Due to the solubility limit of the substrate, the initial concentration of the substrate was adjusted to 20 mM.

Electrocatalytic synthesis of other amino acids

We further extended the substrate scope to verify the applicability of our method and investigate the influence of the keto acid structure on the reaction. A series of aliphatic substrates with increasing carbon chain lengths (Table 1, entries 1–6) and aromatic substrates (Table 1, entries 7–9) were used to produce the corresponding amino acids. Interestingly, in contrast to literature reports showing that the low solubility of organic compounds or steric hindrance of substrates caused by long carbon chains would decrease the formation rate,[23,44,45,47,48,64] the substitution of hydrophobic functional groups or elongation of the carbon chain was observed to promote the formation rate in our case. The highest formation rate of 166.9 mmol g^{-1}_{cat} h^{-1} was achieved with norvaline. This suggests that higher hydrophobicity of a keto acid accelerated the formation of the corresponding amino acid, presumably due to the enhancement of the adsorption of the organic species on the hydrophobic BM3 h–CNT (Fig. S14†). To validate this hypothesis, the CV analyses of keto acids were carried out under the reaction conditions, showing that keto acids with larger adsorption peak areas in the CV curves exhibited higher amino acid formation rates (Fig. S15 and S16†). In addition, as shown in the LSV curves (Fig. S17†), the trend of the current densities for different substrates is roughly consistent with the trend of the corresponding formation rates.

Conclusions

We have developed an electrosynthetic route to produce amino acids from α-keto acids with moderate to high FEs and formation rates using ball milled CNTs as the catalyst. Under the optimum reaction conditions (−0.39 V *vs.* RHE, 100 mM substrate, 6 M NH_3, pH 10), a formation rate of 180.9 mmol g^{-1}_{cat} h^{-1} and a FE of ∼90% were attained for glutamic acid synthesis. The synthetic methodology has been extended to the synthesis of eight other amino acids. In particular, we successfully produced long carbon chain amino acids, whose syntheses are conventionally difficult due to their high steric hindrance. Investigation on the structure–activity relationship of CNTs suggests that the high-density intrinsic defects in the BM–CNTs are likely to be the origin of their superior electrocatalytic activity. Electrokinetic studies imply that the pathway of the ERA involves the direct reduction of *in situ* formed imino acids. Further efforts are needed to elucidate the type of defects and their specific ERA activities.

Author contributions

N. Y., L. W., and Y. X. designed the study. Y. X. performed most of the experiments. N. Y., L. W., Y. X., C. W. L., J. C., and Q. Y. were involved in data collection and discussion. N. Y., L. W., Y. X., and C. W. L. wrote and edited the paper.

Conflicts of interest

The authors declare no conflict of interest.

Acknowledgements

This work was supported by the National Research Foundation Singapore NRF Investigatorship (Award No. NRF-NRFI07–2021–0006). We express our gratitude to Dr Zeliang Yuan for performing XPS measurements. We appreciate Zhicheng Liu for the help with TEM imaging. We thank Yanqiu Lu for conducting contact angle measurements.

References

1 A. Karau and I. Grayson, in *Biotechnology of Food and Feed Additives*, ed. H. Zorn and P. Czermak, Springer Berlin Heidelberg, Berlin, Heidelberg, 2014, pp. 189–228, DOI: 10.1007/10_2014_269.

2 N. Tonouchi and H. Ito, *Adv. Biochem. Eng./Biotechnol.*, 2017, **159**, 3–14.

3 *Global Amino Acids Market Size & Share Report, 2022–2030*.

4 M. D'Este, M. Alvarado-Morales and I. Angelidaki, *Biotechnol. Adv.*, 2018, **36**, 14–25.

5 Y.-X. Huo, in *Engineering Microbial Metabolism for Chemical Synthesis*, WORLD SCIENTIFIC (EUROPE), 2017, pp. 69–95, DOI: 10.1142/9781786344304_000310.1142/9781786344304_0003.

6 A. Strecker, *Justus Liebigs Ann. Chem.*, 1850, **75**, 27–45.

7 M. S. Gibson and R. W. Bradshaw, *Angew. Chem., Int. Ed. Engl.*, 1968, **7**, 919–930.

8 T. Parker Eric, J. Cleaves Henderson, P. Dworkin Jason, P. Glavin Daniel, M. Callahan, A. Aubrey, A. Lazcano and L. Bada Jeffrey, *Proc. Natl. Acad. Sci. U. S. A.*, 2011, **108**, 5526–5531.

9 J. Clayden, N. Greeves and S. G. Warren, *Organische Chemie*, Springer, 2013, vol. 2.

10 K. Harada and K. Matsumoto, *J. Org. Chem.*, 1967, **32**, 1794–1800.

11 R. Kadyrov and T. H. Riermeier, *Angew. Chem., Int. Ed.*, 2003, **42**, 5472–5474.

12 S. Ogo, K. Uehara, T. Abura and S. Fukuzumi, *J. Am. Chem. Soc.*, 2004, **126**, 3020–3021.

13 O.-Y. Lee, K.-L. Law, C.-Y. Ho and D. Yang, *J. Org. Chem.*, 2008, **73**, 8829–8837.

14 A. F. Abdel-Magid, K. G. Carson, B. D. Harris, C. A. Maryanoff and R. D. Shah, *J. Org. Chem.*, 1996, **61**, 3849–3862.

15 R. F. Borch, M. D. Bernstein and H. D. Durst, *J. Am. Chem. Soc.*, 1971, **93**, 2897–2904.

16 R. J. Mattson, K. M. Pham, D. J. Leuck and K. A. Cowen, *J. Org. Chem.*, 1990, **55**, 2552–2554.

17 G. Chieffi, M. Braun and D. Esposito, *ChemSusChem*, 2015, **8**, 3590–3594.

18 G. Hahn, P. Kunnas, N. de Jonge and R. Kempe, *Nat. Catal.*, 2019, **2**, 71–77.

19 Y. Nakamura, K. Kon, A. S. Touchy, K.-I. Shimizu and W. Ueda, *ChemCatChem*, 2015, **7**, 921–924.

20 X. Jv, S. Sun, Q. Zhang, M. Du, L. Wang and B. Wang, *ACS Sustainable Chem. Eng.*, 2020, **8**, 1618–1626.

21 G. Liang, A. Wang, L. Li, G. Xu, N. Yan and T. Zhang, *Angew. Chem.*, 2017, **129**, 3096–3100.

22 S. Song, Y. Wang and N. Yan, *Mol. Catal.*, 2018, **454**, 87–93.

23 M. Chatterjee, T. Ishizaka and H. Kawanami, *Green Chem.*, 2016, **18**, 487–496.

24 Y. Chi, Y. G. Zhou and X. Zhang, *J. Org. Chem.*, 2003, **68**, 4120–4122.

25 H. Duan and F. Wang, *Chem. Catal.*, 2022, **2**, 641–643.

26 H. Zhou, Z. Li, L. Ma and H. Duan, *ChemComm*, 2022, **58**, 897–907.

27 K. Li and Y. Sun, *Chem. – Eur. J.*, 2018, **24**, 18258–18270.

28 F. J. Holzhäuser, J. B. Mensah and R. Palkovits, *Green Chem.*, 2020, **22**, 286–301.

29 X. Liu, D. C. Y. Leong and Y. Sun, *Green Chem.*, 2020, **22**, 6531–6539.

30 X. Shang, Y. Yang and Y. Sun, *Green Chem.*, 2020, **22**, 5395–5401.

31 M. T. Bender, X. Yuan, M. K. Goetz and K.-S. Choi, *ACS Catal.*, 2022, **12**, 12349–12368.

32 Y. Xie, P. Ou, X. Wang, Z. Xu, Y. C. Li, Z. Wang, J. E. Huang, J. Wicks, C. McCallum, N. Wang, Y. Wang, T. Chen, B. T. W. Lo, D. Sinton, J. C. Yu, Y. Wang and E. H. Sargent, *Nat. Catal.*, 2022, **5**, 564–570.

33 Z. Xu, M. Sun, Z. Zhang, Y. Xie, H. Hou, X. Ji, T. Liu, B. Huang and Y. Wang, *ChemCatChem*, 2022, **14**, e202200052.

34 Y. Yang, M. Z. Ertem and L. Duan, *Chem. Sci.*, 2021, **12**, 4779–4788.

35 C. W. Li, J. Ciston and M. W. Kanan, *Nature*, 2014, **508**, 504–507.

36 Y. Chen, C. W. Li and M. W. Kanan, *J. Am. Chem. Soc.*, 2012, **134**, 19969–19972.

37 H. Zou, L. J. Arachchige, W. Rong, C. Tang, R. Wang, S. Tan, H. Chen, D. He, J. Hu, E. Hu, C. Sun and L. Duan, *Adv. Funct. Mater.*, 2022, **32**, 2200333.

38 Y. Ma, T. Yang, H. Zou, W. Zang, Z. Kou, L. Mao, Y. Feng, L. Shen, S. J. Pennycook, L. Duan, X. Li and J. Wang, *Adv. Mater.*, 2020, **32**, 2002177.

39 Y. J. Jang and K.-S. Choi, *J. Mater. Chem. A*, 2020, **8**, 13842–13851.

40 H. Zou, W. Rong, B. Long, Y. Ji and L. Duan, *ACS Catal.*, 2019, **9**, 10649–10655.

41 W. Sui, W. Li, Z. Zhang, W. Wu, Z. Xu and Y. Wang, *J. Power Sources*, 2023, **556**, 232438.

42 X. Min, Y. Chen and M. W. Kanan, *Phys. Chem. Chem. Phys.*, 2014, **16**, 13601–13604.

43 T. Sönmez, K. S. Belthle, A. Iemhoff, J. Uecker, J. Artz, T. Bisswanger, C. Stampfer, H. H. Hamzah, S. A. Nicolae, M.-M. Titirici and R. Palkovits, *Catal. Sci. Technol.*, 2021, **11**, 6191–6204.

44 E. Jeffery and A. Meisters, *Aust. J. Chem.*, 1978, **31**, 73–78.

45 E. Jeffery, O. Johansen and A. Meisters, *Aust. J. Chem.*, 1978, **31**, 79–84.

46 J. J. Roylance and K.-S. Choi, *Green Chem.*, 2016, **18**, 5412–5417.

47 S. D. Mürtz, N. Kurig, F. J. Holzhäuser and R. Palkovits, *Green Chem.*, 2021, **23**, 8428–8433.

48 T. Fukushima and M. Yamauchi, *ChemComm*, 2019, **55**, 14721–14724.

49 T. Fukushima and M. Yamauchi, *J. Appl. Electrochem.*, 2021, **51**, 99–106.

50 K. Yan, M. L. Huddleston, B. A. Gerdes and Y. Sun, *Green Chem.*, 2022, **24**, 5320–5325.

51 Z. Liu, Z. Zhao, Y. Wang, S. Dou, D. Yan, D. Liu, Z. Xia and S. Wang, *Adv. Mater.*, 2017, **29**, 1606207.

52 S. Wang, E. Iyyamperumal, A. Roy, Y. Xue, D. Yu and L. Dai, *Angew. Chem., Int. Ed.*, 2011, **50**, 11756–11760.

53 S. Wang, L. Zhang, Z. Xia, A. Roy, D. W. Chang, J.-B. Baek and L. Dai, *Angew. Chem., Int. Ed.*, 2012, **51**, 4209–4212.

54 B. Kumar, M. Asadi, D. Pisasale, S. Sinha-Ray, B. A. Rosen, R. Haasch, J. Abiade, A. L. Yarin and A. Salehi-Khojin, *Nat. Commun.*, 2013, **4**, 2819.

55 Y. Liu, S. Chen, X. Quan and H. Yu, *J. Am. Chem. Soc.*, 2015, **137**, 11631–11636.

56 Y. Liu, Y. Zhang, K. Cheng, X. Quan, X. Fan, Y. Su, S. Chen, H. Zhao, Y. Zhang and H. Yu, *Angew. Chem.*, 2017, **129**, 15813–15817.

57 J. Wu, S. Ma, J. Sun, J. I. Gold, C. Tiwary, B. Kim, L. Zhu, N. Chopra, I. N. Odeh, R. Vajtai, A. Z. Yu, R. Luo, J. Lou, G. Ding, P. J. A. Kenis and P. M. Ajayan, *Nat. Commun.*, 2016, **7**, 13869.

58 G. Gan, S. Fan, X. Li, J. Wang, C. Bai, X. Guo, M. Tade and S. Liu, *ACS Catal.*, 2021, **11**, 14284–14292.

59 X. Zhang, H. Jing, S. Chen, B. Liu, L. Yu, J. Xiao and D. Deng, *Chem. Catal.*, 2022, **2**, 1–2.

60 M. J. Matthews, M. A. Pimenta, G. Dresselhaus, M. S. Dresselhaus and M. Endo, *Phys. Rev. B: Condens. Matter Mater. Phys.*, 1999, **59**, R6585–R6588.

61 L. G. Bulusheva, A. V. Okotrub, I. A. Kinloch, I. P. Asanov, A. G. Kurenya, A. G. Kudashov, X. Chen and H. Song, *Phys. Status Solidi B*, 2008, **245**, 1971–1974.

62 A. Anne, S. Daninos and J. Moiroux, *New J. Chem.*, 1994, **18**, 1169–1174.

63 H. Lund, *Acta Chem. Scand.*, 1959, **13**, 249–267.

64 T. Pienemann and H. J. Schäfer, *Synthesis*, 1987, 1005–1007.

65 J. Wu, M. Liu, P. P. Sharma, R. M. Yadav, L. Ma, Y. Yang, X. Zou, X.-D. Zhou, R. Vajtai, B. I. Yakobson, J. Lou and P. M. Ajayan, *Nano Lett.*, 2016, **16**, 466–470.

66 J. Wu, S. Ma, J. Sun, J. I. Gold, C. Tiwary, B. Kim, L. Zhu, N. Chopra, I. N. Odeh and R. Vajtai, *Nat. Commun.*, 2016, **7**, 1–6.

67 J. Wu, R. M. Yadav, M. Liu, P. P. Sharma, C. S. Tiwary, L. Ma, X. Zou, X.-D. Zhou, B. I. Yakobson, J. Lou and P. M. Ajayan, *ACS Nano*, 2015, **9**, 5364–5371.

68 R. M. Yadav, Z. Li, T. Zhang, O. Sahin, S. Roy, G. Gao, H. Guo, R. Vajtai, L. Wang and P. M. Ajayan, *Adv. Mater.*, 2022, **34**, 2105690.

69 W. Tian, C. Wang, R. Chen, Z. Cai, D. Zhou, Y. Hao, Y. Chang, N. Han, Y. Li, J. Liu, F. Wang, W. Liu, H. Duan and X. Sun, *RSC Adv.*, 2018, **8**, 26004–26010.

70 B. J. Matsoso, K. Ranganathan, B. K. Mutuma, T. Lerotholi, G. Jones and N. J. Coville, *RSC Adv.*, 2016, **6**, 106914–106920.